Alleviating cosmological tensions with a coupled scalar fields model

Gang Liu,* Zhihuan Zhou, Yuhao Mu, and Lixin Xu†
Institute of Theoretical Physics, School of Physics, Dalian University of Technology, Dalian 116024, People's Republic of China

(Received 18 April 2023; accepted 2 September 2023; published 20 October 2023)

In this paper, we investigate the interaction between early dark energy (EDE) and scalar field dark matter, proposing a coupled scalar fields model to address the Hubble tension and S_8 tension. While the EDE model successfully alleviates the Hubble tension, it exacerbates the S_8 tension. To mitigate the negative impact of EDE, we introduce the interaction between EDE and dark matter. Specifically, we replace cold dark matter with scalar field dark matter, given its capability to suppress structure growth on small scales. We constrained the new model using cosmological observations including the temperature and polarization anisotropy power spectra data of cosmic microwave background radiation from *Planck* 2018 results, baryon acoustic oscillations measurements extracted from 6dFGS, SDSS, and BOSS, the Pantheon sample of type Ia supernovae, the local distance-ladder data (SH0ES), and the Dark Energy Survey Year-3 data. Employing the Markov Chain Monte Carlo method, we find that this novel model yields best-fit values of H_0 and S_8 equal to 71.13 km/s/Mpc and 0.8256, respectively. Compared to the ΛCDM model, the new model alleviates the Hubble tension but still fails to resolve the S_8 tension. However, we obtain a smaller value of S_8 compared to the result of 0.8316 obtained for EDE model, which mitigates to some extent the shortcoming of the EDE model.

DOI: 10.1103/PhysRevD.108.083523

I. INTRODUCTION

Over the past few years, the ΛCDM model has encountered numerous challenges as a result of the growing quantity and quality of observations. The emergence of the Hubble tension and the S_8 tension has garnered significant attention. The Hubble tension [1] pertains to the discrepancy between the H_0 value obtained from model-independent local measurements such as Type Ia supernovae (SNIa) [2,3], and the H_0 value derived from the cosmic microwave background (CMB) [4] and the large-scale structure (LSS) [5–8]. More precisely, the *Planck* 2018 CMB data estimates the value of H_0 to be 67.37 ± 0.54 km/s/Mpc [4], while the cosmic distance ladder measurement (SH0ES) yields $H_0 = 73.04 \pm 1.04$ km/s/Mpc [9], with a statistical error of 4.8σ.

The S_8 tension characterizes the inconsistency between CMB and LSS observations [10,11]. The *Planck* best-fit ΛCDM model estimates the value of S_8 to be 0.834 ± 0.016 [4], while LSS observations yield $0.759^{+0.024}_{-0.021}$ for KiDS-1000 [12], $0.800^{+0.029}_{-0.028}$ for HSC-Y1 [13], and 0.776 ± 0.017 for Dark Energy Survey Year-3 (DES-Y3) [14].

Numerous models have been proposed to address the Hubble tension, as reviewed recently by [15]. These models incorporate modifications to the late Universe, such as the phenomenologically emergent dark energy model [16], the phantom transition [17], and the early Universe, including the early dark energy (EDE) model [18–20], the acoustic dark energy model [21], and the new early dark energy model [22], etc.

Despite the proposed models, they still encounter several issues. For instance, the late-time solutions that do not alter the sound horizon are generally unable to account for the SH0ES measurement. Conversely, the early-time solutions that introduce a new component before recombination to decrease the scale of the acoustic horizon on the final scattering surface, increase the value of H_0, and maintain the angular scale of the acoustic horizon in CMB observations, but they exacerbate the S_8 tension [20].

This paper focuses on the EDE model and aims to address the associated concerns. EDE is characterized by an ultralight axion scalar field [23,24]. In this model, z_c denotes the redshift at the apex of the EDE component contribution, while f_{EDE} represents the proportion of EDE energy density relative to the total energy density at that time. The evolution of the EDE fraction with the redshift is depicted in Fig. 1, where the red vertical dashed line denotes the redshift at recombination, and the apex of the EDE component occurs before recombination. The Hubble tension can be resolved when the EDE ratio f_{EDE} reaches approximately 10% [20].

During its contribution period, the EDE component marginally diminishes the perturbed growth of the structure. To align with the CMB data, the cold dark matter

*liugang_dlut@mail.dlut.edu.cn
†lxxu@dlut.edu.cn

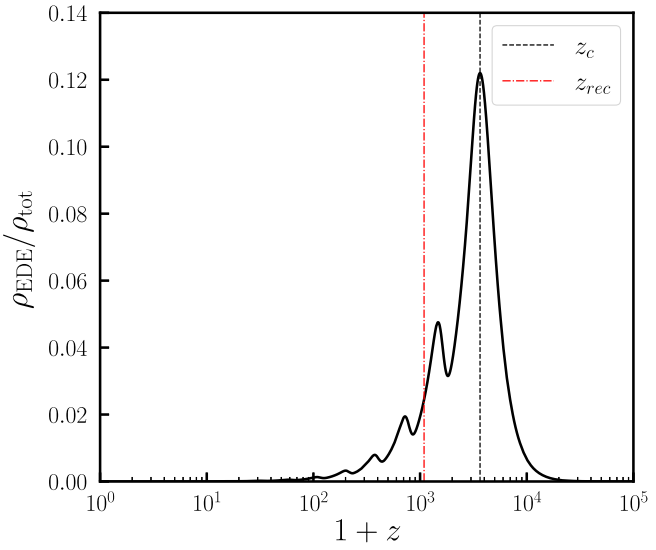

FIG. 1. The evolution of the EDE energy density as a fraction of the total energy density with respect to the redshift. The red vertical dash-dotted line corresponds to the redshift at recombination $z_{\rm rec}$, while the black vertical dashed line represents the critical redshift of EDE.

(CDM) density must be augmented to offset these losses. Moreover, some other cosmological parameters, such as the scalar spectral index n_s, the baryon density ω_b, and the amplitude of density perturbations σ_8, will also undergo changes [25]. Consequently, the EDE model will invariably exacerbate the CMB-LSS inconsistency [20,26].

To reduce the S_8 tension, it is common to investigate the interaction of dark matter (DM) and dark energy (DE), which can inhibit the growth of structure through the drag of DE on DM [27,28]. In addition, since the nature of dark matter is not yet comprehensively understood, alternative descriptions can be developed to substitute cold dark matter, and alleviate the S_8 tension.

The ΛCDM model posits that dark matter is comprised of nonbaryonic, pressureless, and nonrelativistic particles [29]. This model has been successful in explaining large-scale observations from the cosmic microwave background (CMB) and large-scale structure (LSS). However, despite its achievements, the microscopic properties of dark matter remain unknown [30]. The aforementioned assumptions have led to a number of unresolved issues, such as the unexpected behavior of central densities in galactic halos and the overpopulation of secondary structures on small scales. These observations suggest that the cold dark matter may not be an adequate description of dark matter, particularly on smaller scales [29].

Scalar field dark matter (SFDM) presents an alternative to cold dark matter, which is composed of a light scalar field with a mass of approximately 10^{-22} eV [29,30]. In this model, the scalar field forms a Bose-Einstein condensate at the galactic scale, which modifies the dynamics of dark matter on small scales while maintaining the success of cold dark matter on large scales. This condensation leads to the suppression of structure growth on small scales, which could potentially alleviate the S_8 tension.

The behavior of the scalar field dark matter is similar to that of the cosmological constant in the early Universe, followed by oscillations, and ultimately similar to CDM. Figure 2 displays the evolution of the SFDM equation of state with the redshift. The initiation time of the oscillations is determined by the field mass. A smaller mass results in later oscillations.

This paper proposes a coupled scalar fields (CSF) model that explores the interaction between early dark energy and scalar field dark matter. The coupling between the two fields is inspired by the swampland distance conjecture (SDC) [31,32], which has previously been applied to quintessence models [33] and the EDE model [25]. According to the SDC, a low-energy effective field theory is deemed valid only within a region of field space constrained by the Planck scale. Moreover, any breakdown of the effective field theory that arises due to Planckian field excursions can be expressed as an exponential sensitivity reflected in the mass spectrum of the effective theory. Specifically, the CSF model posits that the mass of dark matter is exponentially dependent on the EDE scalar,

$$m_{\rm DM}(\phi) = m_0 e^{\beta\phi/M_{pl}}, \tag{1}$$

where, m_0 represents the present-day mass of dark matter, ϕ denotes the EDE scalar, $\beta \sim \mathcal{O}(1)$ is a constant, and $M_{pl} = 2.435 \times 10^{27}$ eV denotes the reduced Planck mass.

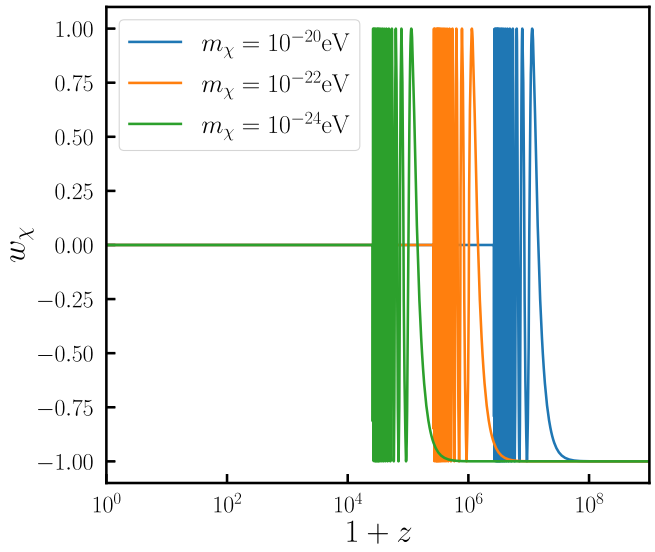

FIG. 2. The equation of state of scalar field dark matter is presented as a function of the redshift for various masses. Initially, SFDM behaves like the cosmological constant, followed by oscillations, and ultimately evolves into a behavior similar to cold dark matter. The initiation time of the oscillations is dependent on the field mass.

In this study, we have conducted a comprehensive investigation into the evolutionary equations of the coupled model at both the background and perturbation levels. We employed a Markov Chain Monte Carlo (MCMC) analysis of three cosmological models, namely the ΛCDM, EDE, and CSF models. We utilized various datasets, including the *Planck* 2018 primary CMB data and CMB lensing data [4,34,35], baryon acoustic oscillation measurements from the BOSS DR12, the 6dF galaxy survey, and SDSS DR7 [36–39], the Pantheon supernovae Ia data [40], the SH0ES measurement [9], and the Dark Energy Survey Year-3 data [14].

Based on the entire datasets, we found that the H_0 values obtained by the EDE and CSF models are 72.46 ± 0.86 km/s/Mpc and 72.20 ± 0.81 km/s/Mpc at a 68% CL, respectively, both exceeding the result of $68.71^{+0.35}_{-0.41}$ km/s/Mpc obtained by the ΛCDM model. Therefore, both models can alleviate the Hubble tension. The S_8 value for the EDE model is $0.822^{+0.011}_{-0.0093}$, while the result for CSF is $0.820^{+0.014}_{-0.008}$. Furthermore, the obtained coupling constant is constrained to be -0.014 ± 0.016, indicating an interaction between dark matter and dark energy. Despite the failure of the coupled model to resolve the S_8 tension, it has yielded a smaller S_8 and $\chi^2_{\rm tot}$ compared to the EDE model, thereby mitigating the adverse effect associated with EDE.

The paper is organized as follows. Section II presents an introduction to the CSF model, including the dynamics of background and perturbation. In Sec. III, we present numerical results illustrating the impact of the coupled model on the large-scale structures. In Sec. IV, we discuss the datasets utilized in our analysis and present the corresponding results. Finally, we summarize our findings in Sec. V.

II. COUPLED SCALAR FIELDS

We examine the coupling between SFDM and EDE. The Lagrangian is defined as follows:

$$\mathcal{L} = -\frac{1}{2}\partial^\mu\chi\partial_\mu\chi - \frac{1}{2}m_\chi(\phi)^2\chi^2 - \frac{1}{2}\partial^\mu\phi\partial_\mu\phi - V(\phi), \tag{2}$$

where ϕ is the EDE scalar with the potential [20]

$$V(\phi) = m_\phi^2 f_\phi^2[1-\cos(\phi/f_\phi)]^3 + V_\Lambda, \tag{3}$$

and χ is SFDM scalar with a ϕ-dependent mass $m_\chi(\phi)$, V_Λ in Eq. (3) serves as the cosmological constant. The subscript ϕ is used to denote dark energy and χ is used to denote dark matter. Numerous potentials of SFDM have been investigated in previous studies [41,42], but the common features of them can be represented by $\frac{1}{2}m_\chi^2\chi^2$ [43]. The specific form of $m_\chi(\phi)$ is

$$m_\chi(\phi) = m_0 e^{\beta\phi/M_{pl}}, \tag{4}$$

which is given by the swampland distance conjecture as Eq. (1), and m_0 represents the present-day mass of SFDM.

A. Background equations

The motion equations of the scalar field dark matter in a flat Friedmann-Lemaître-Robertson-Walker cosmology can be expressed as follows:

$$3M_{pl}^2H^2 = \sum_I \rho_I, \tag{5a}$$

$$-2M_{pl}^2\dot{H} = \sum_I \rho_I + p_I, \tag{5b}$$

$$\ddot{\chi} = -3H\dot{\chi} - m_\chi^2\chi, \tag{5c}$$

where the dot denotes the derivative with respect to cosmic time, and H is the Hubble parameter, ρ_I and p_I are the energy density and pressure for each component respectively. The expressions for the energy density and pressure of SFDM are as follows:

$$\rho_\chi = \frac{1}{2}\dot{\chi}^2 + \frac{1}{2}m_\chi^2\chi^2, \tag{6a}$$

$$p_\chi = \frac{1}{2}\dot{\chi}^2 - \frac{1}{2}m_\chi^2\chi^2. \tag{6b}$$

We define a new set of variables to transform the Klein-Gordon equation (5c) [44],

$$x = \frac{\dot{\chi}}{\sqrt{6}M_{pl}H}, \qquad y = -\frac{m_\chi\chi}{\sqrt{6}M_{pl}H}, \qquad y_1 = \frac{2m_\chi}{H}. \tag{7}$$

We utilize the polar coordinate variable transformation form as proposed in previous works [43–45],

$$x = \sqrt{\Omega_\chi}\sin\frac{\theta}{2}, \qquad y = \sqrt{\Omega_\chi}\cos\frac{\theta}{2}, \tag{8}$$

where $\Omega_\chi = \frac{\rho_\chi}{3M_{pl}^2H^2}$ is the density parameter of the dark matter. The Friedman equations (5) and (5b) are reformulated as follows:

$$\frac{\dot{H}}{H^2} = -\frac{3}{2}(1+w_t), \qquad 1 = \sum_I \Omega_I + \Omega_\chi, \tag{9}$$

where $w_t = \frac{p_t}{\rho_t}$ represents the total equation of state, which is the ratio of total pressure p_t to total energy density ρ_t, and $\Omega_I = \frac{\rho_I}{3M_{pl}^2H^2}$ is the density parameter of each components. The Klein-Gordon equation (5c) becomes

$$\frac{\dot{\Omega}_\chi}{\Omega_\chi} = 3H(w_t + \cos\theta) + \frac{\beta\dot{\phi}}{M_{pl}}(1+\cos\theta), \quad (10a)$$

$$\dot{\theta} = H(y_1 - 3\sin\theta) - \frac{\beta\dot{\phi}}{M_{pl}}\sin\theta, \quad (10b)$$

$$\dot{y_1} = \frac{3}{2}H(1+w_t)y_1 + \frac{\beta\dot{\phi}}{M_{pl}}y_1. \quad (10c)$$

The equations of motion for the EDE is given by the variation of the action expanded to linear order in $\delta\phi$,

$$\ddot{\phi} + 3H\dot{\phi} + \frac{dV}{d\phi} = -3\beta M_{pl}H^2\Omega_\chi(1+\cos\theta). \quad (11)$$

The left panel of Fig. 3 depicts the evolution of the EDE scalar, while the right panel shows the EDE energy density fraction as a function of the redshift across various coupling constants. The cosmological parameters utilized in this analysis are derived from the best-fit values listed in Table I. The amplitude and phase of the EDE scalar will be altered by varying coupling constants. The sign of the coupling constant determines the direction of conversion between dark matter and dark energy components. A negative coupling constant results in a source term on the right-hand side of Eq. (11), causing the conversion of dark matter into dark energy and leading to an increase in the energy density fraction of EDE. Conversely, a positive coupling constant causes the conversion of dark energy into dark matter.

The energy density and pressure of the EDE are

$$\rho_\phi = \frac{1}{2}\dot{\phi}^2 + V(\phi), \quad (12a)$$

$$p_\phi = \frac{1}{2}\dot{\phi}^2 - V(\phi). \quad (12b)$$

The equations of continuity for SFDM and EDE can be derived from the Klein-Gordon equations presented in Eq. (5c) and Eq. (11), respectively,

$$\dot{\rho_\chi} = -3H(\rho_\chi + p_\chi) + \frac{\beta\dot{\phi}}{M_{pl}}(1+\cos\theta)\rho_\chi, \quad (13a)$$

$$\dot{\rho_\phi} = -3H(\rho_\phi + p_\phi) - \frac{\beta\dot{\phi}}{M_{pl}}(1+\cos\theta)\rho_\chi. \quad (13b)$$

Many coupled dark energy models have this common form [46–50], which ensures covariant conservation for the total stress tensor.

B. Perturbation equations

We calculated the perturbation equation using the synchronous gauge, where the metric is defined as follows:

$$ds^2 = -dt^2 + a^2(t)(\delta_{ij} + h_{ij})dx^i dx^j. \quad (14)$$

The scalars of SFDM and EDE are given by

$$\chi(x,t) = \chi(t) + \delta\chi(x,t), \quad (15a)$$

$$\phi(x,t) = \phi(t) + \delta\phi(x,t), \quad (15b)$$

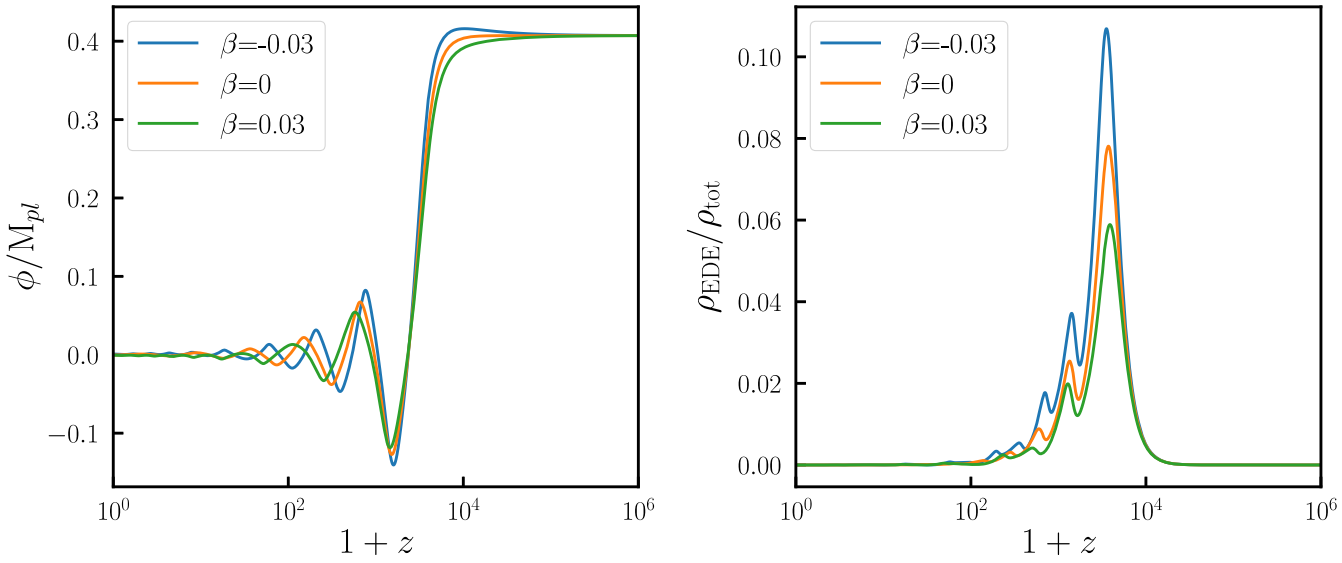

FIG. 3. The variation of the EDE scalar (in the left panel) and the EDE energy density fraction (in the right panel) as functions of the redshift, for different coupling constants. The negative (positive) coupling constant leads to the conversion of the dark matter (dark energy) component into dark energy (dark matter), increasing (decreasing) the EDE energy density fraction.

with $\chi(t)$, $\phi(t)$ the background parts, and $\delta\chi(x,t)$, $\delta\phi(x,t)$ the linear perturbations, respectively.

The perturbed Klein-Gordon equation for a Fourier mode of $\delta\chi(x,t)$ is

$$\dot{\delta\chi} = -3H\delta\chi - \left(\frac{k^2}{a^2} + m_\chi^2\right)\delta\chi - \frac{1}{2}\dot{\chi}\,\dot{h}, \tag{16}$$

where h representes the trace of scalar metric perturbations. The density perturbations $\delta\rho(\chi)$, pressure perturbations $\delta p(\chi)$, and velocity divergence $\Theta(\chi)$ can be expressed as provided in [51,52],

$$\delta\rho_\chi = \dot{\chi}\,\dot{\delta\chi} + \partial_\chi V(\chi)\delta\chi, \tag{17a}$$

$$\delta p_\chi = \dot{\chi}\,\dot{\delta\chi} - \partial_\chi V(\chi)\delta\chi, \tag{17b}$$

$$(\rho_\chi + p_\chi)\Theta_\chi = \frac{k^2}{a}\dot{\chi}\delta\chi. \tag{17c}$$

As previously done in the background section, we introduce new variables to derive the perturbation equation [45],

$$u = \sqrt{\frac{2}{3}}\frac{\dot{\delta\chi}}{M_{pl}H} = -\sqrt{\Omega_\chi}e^\alpha\cos\frac{\vartheta}{2}, \tag{18a}$$

$$v = \sqrt{\frac{2}{3}}\frac{m_\chi\delta\chi}{M_{pl}H} = -\sqrt{\Omega_\chi}e^\alpha\sin\frac{\vartheta}{2}. \tag{18b}$$

Once more, we introduce a new set of variables,

$$\delta_0 = -e^\alpha\sin\left(\frac{\theta}{2} - \frac{\vartheta}{2}\right), \tag{19a}$$

$$\delta_1 = -e^\alpha\cos\left(\frac{\theta}{2} - \frac{\vartheta}{2}\right). \tag{19b}$$

The equations of motion for the new variables are

$$\dot{\delta_0} = \delta_0 H\omega\sin\theta - \delta_1[3H\sin\theta + H\omega(1-\cos\theta)] - \frac{\dot{h}}{2}(1-\cos\theta) - \frac{\beta\dot{\phi}}{M_{pl}}\delta_1\sin\theta, \tag{20a}$$

$$\dot{\delta_1} = \delta_0 H\omega(1+\cos\theta) - \delta_1(3H\cos\theta + H\omega\sin\theta) - \frac{\dot{h}}{2}\sin\theta - \frac{\beta\dot{\phi}}{M_{pl}}\delta_1\cos\theta, \tag{20b}$$

where

$$\omega = \frac{k^2}{2a^2m_\chi H} = \frac{k^2}{a^2H^2y_1}. \tag{21}$$

The relationship between the new variables and density, pressure, and velocity divergence can be established by referring to the definition given in Eq. (17),

$$\delta\rho_\chi = \rho_\chi\delta_0, \tag{22a}$$

$$\delta p_\chi = \rho_\chi(\delta_1\sin\theta - \delta_0\cos\theta), \tag{22b}$$

$$(\rho_\chi + p_\chi)\Theta_\chi = \frac{k^2}{aHy_1}\rho_\chi[\delta_1(1-\cos\theta) - \delta_0\sin\theta]. \tag{22c}$$

Expanding the action to the second order and varying with respect to $\delta\phi$, we obtain the equation of motion for EDE perturbation is

$$\dot{\delta\dot{\phi}} + 3H\dot{\delta\phi} + \frac{1}{2}\dot{h}\,\dot{\phi} + \left(\frac{k^2}{a^2} + \frac{d^2V}{d\phi^2}\right)\delta\phi = \frac{\beta}{M_{pl}}\rho_\chi[\delta_1\sin\theta - \delta_0(1+\cos\theta)] - 2\left(\frac{\beta}{M_{pl}}\right)^2\rho_\chi(1+\cos\theta)\delta\phi. \tag{23}$$

C. Initial conditions

In the early Universe, Hubble friction induces the effective freezing of the scalar fields at their initial value, leading to a slow-roll process. The initial value of $\dot{\phi}$ can be set to 0. And the energy density of dark matter can be approximated to be negligible at that time. As a result, the equations of the EDE and SFDM simplify to an uncoupled form.

We treat the ratio between the initial value of EDE scalar and the axion decay constant, $\alpha_i = \phi_i/f_\phi$ as the model parameter [19,20]. We employ the attractor solution initial conditions for SFDM, namely,

$$\theta_i = \frac{2}{5}\frac{m_0 e^{\frac{\beta\phi_i}{M_{pl}}}}{H_0\sqrt{\Omega_r a_i^{-4}}}, \tag{24a}$$

$$y_{1i} = 5\theta_i, \tag{24b}$$

where Ω_r represents the energy density fraction of the present radiation component, and a_i denotes the initial value of the scale factor. The initial value of Ω_χ is calculated using the widely employed shooting algorithm in the Boltzmann code CLASS [53,54], based on the current value of the energy density of dark matter. The specific deductive process can be found in reference [43,55], for further details. It should be noted that in the new model, the mass of SFDM is ϕ-dependent. Therefore, the value of θ_i need to be adjusted accordingly. We adopt adiabatic initial conditions for the perturbation equations of EDE and SFDM, for a detailed description, please refer to [19,55].

III. NUMERICAL RESULTS

The publicly available Boltzmann code CLASS [53,54] was modified as described in Sec. II. We replace cold dark matter with SFDM as the constituent of dark matter. In order to compute various perturbation equations using the synchronous gauge in CLASS, we set the energy density fraction of cold dark matter, $\Omega_{\mathrm{cdm},0}$ to a value of 10^{-6} [43]. We performed computations of the CMB power spectrum and the matter power spectrum by employing the existing spectrum module of CLASS.

We investigate the impact of the new model on the tension of large-scale structures. Figure 4 displays the evolution of $f\sigma_8(z)$ with the redshift for three models, each with the corresponding best-fit values taken from Table I. The ΛCDM, EDE, and CSF models are depicted by dashed black, dash-dotted blue, and solid orange lines, respectively. The 63 observed Redshift Space Distortion $f\sigma_8(z)$ data points are collected from [56].

Compared to the ΛCDM model, both the EDE and CSF models yield larger values of $f\sigma_8$, exacerbating the S_8 tension. However, the results of the CSF model are slightly smaller than those of the EDE model. This discrepancy primarily stems from the inhibitory influence of SFDM on structure growth on small scales. We can more distinctly observe this characteristic in the matter power spectrum.

Figure 5 presents the linear matter power spectra (upper panel) and their relative differences compared to the ΛCDM model (lower panel) for three models. All parameters are obtained from the best-fit values in Table I. Due to the interplay between dark matter and dark energy, as well as the condensation effect of SFDM, the matter power spectrum obtained from the CSF model is smaller than that of the EDE model on small scales, indicating suppressed growth of structures and thus alleviating the S_8 tension caused by EDE. It is worth noting that the CSF model still obtains a larger power spectrum on small scales compared to the ΛCDM model, thus we have not resolved the S_8 tension completely.

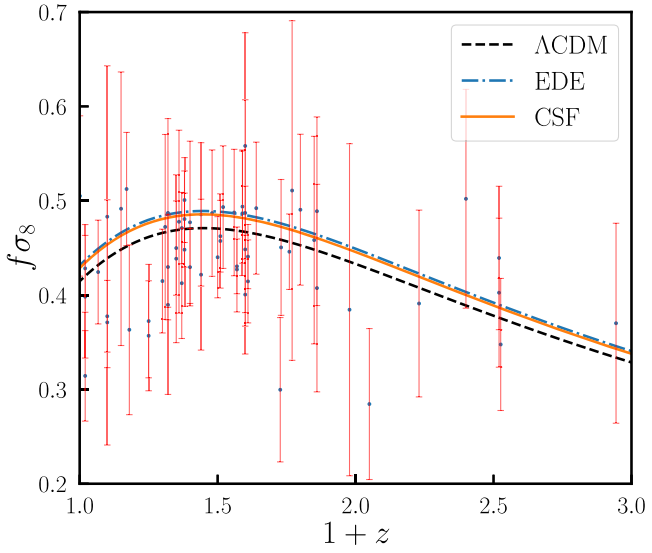

FIG. 4. The evolution of $f\sigma_8(z)$ with the redshift for different models, namely the ΛCDM model (dashed black line), the EDE model (dash-dotted blue line), and the CSF model (solid orange line).

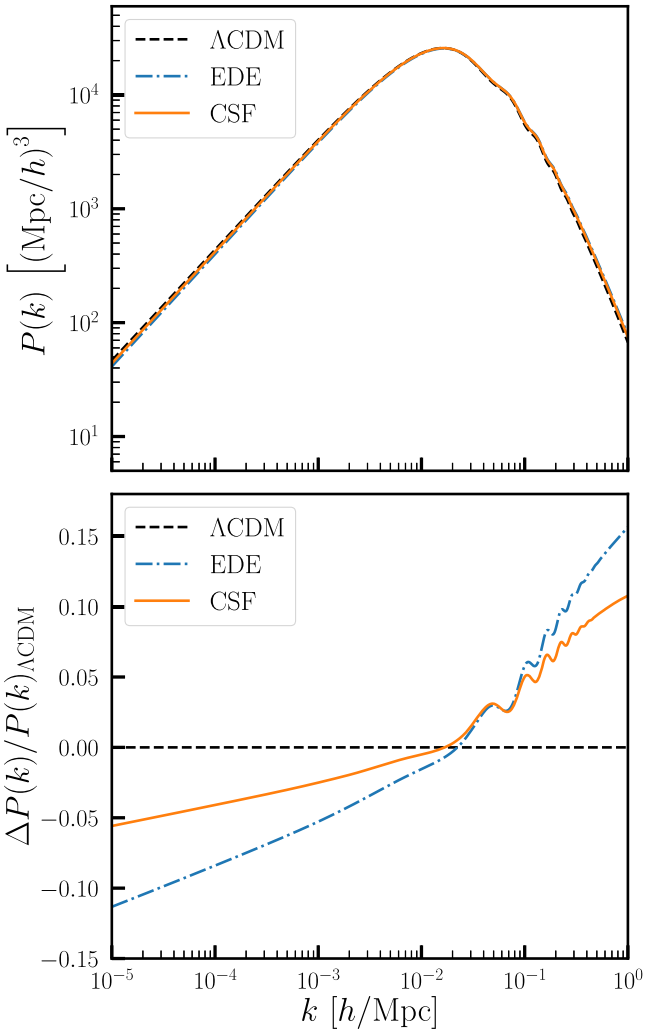

FIG. 5. The linear matter power spectra of three models (upper panel) and their relative values compared to the ΛCDM model (lower panel) are presented. The matter power spectrum obtained from the CSF model is smaller than that of the EDE model on small scales.

IV. CONSTRAINTS AND RESULTS

The MCMC analysis was performed using `MontePython` [57,58], and the MCMC chains were analyzed using GetDist [59]. We conducted the analysis using the following datasets:

(1) *CMB*: The temperature and polarization power spectra from *Planck* 2018 low-ℓ, high-ℓ, and CMB lensing power spectrum [4,34,35].

(2) *BAO*: The measurements from BOSS-DR12 $f\sigma_8$ sample, namely, the combined LOWZ and CMASS galaxy samples [36,37] and the small-z measurements from 6dFGS and the SDSS DR7 [38,39].
(3) *Supernovae*: The Pantheon sample, composed of 1048 supernovae Ia in the redshift range $0.01 < z < 2.3$ [40].
(4) *SH0ES*: The recent SH0ES measurement with $H_0 = 73.04 \pm 1.04$ km/s/Mpc [9].
(5) *DES-Y3*: The $S_8 = 0.776 \pm 0.017$ from Dark Energy Survey Year-3 weak lensing and galaxy clustering data [14].

The results of the parameter constraints are shown in Table I. The upper part of the table enlists the cosmological parameters that underwent sampling in the Markov chain Monte Carlo method. Meanwhile, the lower section exhibits the derived parameters.

We use the complete dataset to ensure convergence for all models, with each parameter achieving the Gelman-Rubin statistic value of $R - 1 < 0.05$ [60].

According to the results presented in Table I, the EDE and CSF models obtained H_0 values of 72.46 ± 0.86 km/s/Mpc and 72.20 ± 0.81 km/s/Mpc at a 68% confidence level, respectively, which are higher than the value of $68.71^{+0.35}_{-0.41}$ km/s/Mpc obtained by the ΛCDM model. This suggests that both the EDE and CSF models can alleviate the Hubble tension.

However, the EDE model and CSF model resulted in larger values of S_8, which further exacerbated the tension with the LSS. We obtained a nonzero coupling constant, β, with a value of -0.014 ± 0.016 at a 68% CL, indicating the interaction between dark components through the conversion of dark matter into dark energy. Combined with the condensation of SFDM on small scales, it is clear from Fig. 6 that the CSF model yields smaller density fluctuation amplitude σ_8 compared to the EDE model, thereby alleviating the S_8 tension caused by the EDE model. The full posterior distribution is shown in Fig. 7 of the Appendix section.

The penultimate row of Table I displays the $\Delta\chi^2_{\rm tot}$ values for the EDE and CSF models relative to the ΛCDM model, which are -11.74 and -13.78, respectively, which is primarily attributed to the data from SH0ES. This indicates that both models fit the data better than the standard model. Furthermore, the $\chi^2_{\rm tot}$ obtained by our new model is smaller than that of the EDE model. This is attributed to the CSF model obtaining a smaller S_8 compared to the EDE model, resulting in a closer alignment with the data from DES-Y3. Thus, from a $\chi^2_{\rm tot}$ perspective, our novel model exhibits the performance.

We also compared the models by calculating the Akaike information criterion (AIC) [61],

$$\mathrm{AIC} = \chi^2_{\rm tot} + 2k, \tag{25}$$

where k represents the number of fitted parameters. The smaller the AIC value of a model, the higher its goodness of fit. The results are presented in the last row of Table I. The ΔAIC values for the EDE and CSF models relative to the ΛCDM model are -5.74 and -3.78, respectively, which indicates that the EDE model has the best fit. Despite the CSF model demonstrating a smaller $\chi^2_{\rm tot}$ value, its performance is slightly inferior to that of the EDE model from the perspective of AIC, primarily due to the incorporation of additional parameters.

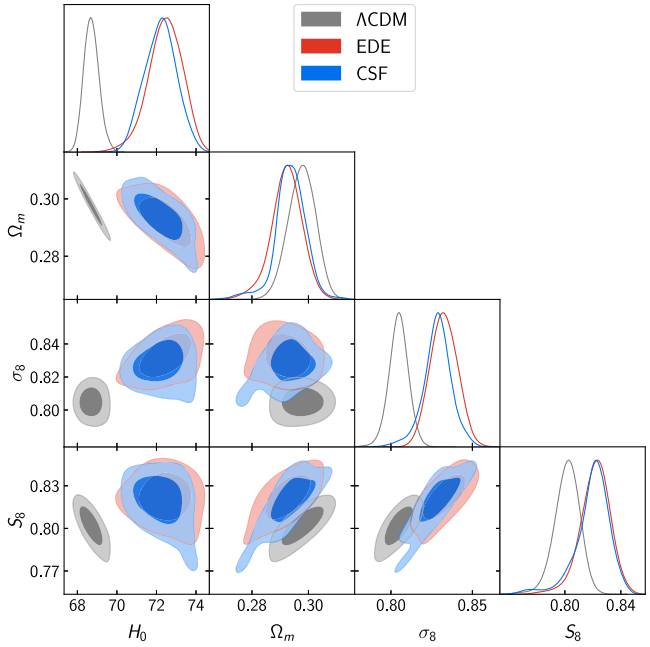

FIG. 6. The posteriors of various models. Compared to the ΛCDM model, both the EDE and CSF models yield larger H_0, and consequently, larger S_8. However, the CSF model partially alleviates the S_8 tension compared to the EDE model. The full posteriors is provided in the appendix.

V. CONCLUSION

This study examines the interplay between early dark energy and scalar field dark matter, proposing a coupled scalar fields model to reconcile the discrepancies in H_0 and S_8 measurements. The CSF model leverages the EDE component to enhance H_0 without compromising the cosmic microwave background observations, additionally, the suppression of SFDM on small-scale structure growth and the drag of dark energy on dark matter can alleviate the extra S_8 tension caused by EDE.

We investigated the evolutionary equations of the coupled model, encompassing both the background and perturbation levels, and explored their impact on the growth of structures and the power spectrum of matter. We then constrain the parameters of the ΛCDM, EDE, and CSF models using the full data including CMB, BAO, SNIa, SH0ES, and S_8 from DES-Y3.

We constrain the coupling constant to be -0.014 ± 0.016 at a 68% CL, indicating the interaction between dark

matter and dark energy. The EDE and CSF models yield H_0 values of 72.46 ± 0.86 km/s/Mpc and 72.20 ± 0.81 km/s/Mpc at a 68% CL, respectively, which are higher than the ΛCDM value of $68.71^{+0.35}_{-0.41}$ km/s/Mpc, thus alleviating the Hubble tension.

In addition, the EDE model and CSF model yield S_8 best-fit values of 0.8316 and 0.8256 respectively, both of which exceed the result of the ΛCDM model at 0.7985, further exacerbating the existing S_8 tension. However, it is notable that the S_8 for the CSF model is lower than that of the EDE model, and the $\chi^2_{\rm tot}$ obtained from fitting the data in the former is also smaller than that in the latter, indicating the potential of the new model to alleviate the negative effect associated with the EDE model. We have also computed the AIC for model comparison. Despite the smaller $\chi^2_{\rm tot}$ of the CSF model, its weaker fit compared to the EDE model can be attributed to the introduction of additional parameters.

ACKNOWLEDGMENTS

This work is supported in part by National Natural Science Foundation of China under Grants No. 12075042 and No. 11675032 (People's Republic of China).

APPENDIX: THE FULL MCMC POSTERIORS

TABLE I. The table presents the best-fit parameters and 68% CL marginalized constraints for ΛCDM, EDE, and CSF models using a combined data comprising CMB, BAO, SNIa, SH0ES, and S_8 from DES-Y3. The upper section of the table lists the cosmological parameters that were sampled in the MCMC, while the lower section displays the derived parameters.

Model	ΛCDM	EDE	CSF
$100\omega_b$	$2.269(2.263 \pm 0.014)$	$2.276(2.281^{+0.024}_{-0.020})$	$2.249(2.278^{+0.023}_{-0.018})$
ω_{dm}	$0.11724(0.11725 \pm 0.00084)$	$0.1310(0.1299 \pm 0.0028)$	$0.1285(0.1282^{+0.0024}_{-0.0028})$
H_0	$68.73(68.71^{+0.35}_{-0.41})$	$71.85(72.46 \pm 0.86)$	$71.13(72.20 \pm 0.81)$
$\ln(10^{10}A_s)$	$3.043(3.050 \pm 0.015)$	$3.057(3.063^{+0.015}_{-0.017})$	$3.058(3.060 \pm 0.016)$
n_s	$0.9736(0.9722 \pm 0.0040)$	$0.9877(0.9908 \pm 0.0059)$	$0.9804(0.9870^{+0.0067}_{-0.0050})$
$\tau_{\rm reio}$	$0.0574(0.0592 \pm 0.0082)$	$0.0539(0.0563 \pm 0.0090)$	$0.0554(0.0561^{+0.0082}_{-0.00035})$
$\log_{10}(m_\phi)$	⋯	$-27.292(-27.290 \pm 0.055)$	$-27.310(-27.287 \pm 0.057)$
$\log_{10}(f_\phi)$	⋯	$26.632(26.616^{+0.056}_{-0.033})$	$26.563(26.643 \pm 0.044)$
α_i	⋯	$2.762(2.783 \pm 0.069)$	$2.712(2.684 \pm 0.053)$
β	⋯	⋯	$-0.027(-0.014 \pm 0.016)$
$\log_{10}(m_\chi)$	⋯	⋯	$-22.092(-22.008^{+0.087}_{-0.070})$
$10^{-9}A_s$	$2.096(2.112 \pm 0.032)$	$2.127(2.139^{+0.031}_{-0.036})$	$2.129(2.133 \pm 0.035)$
$100\theta_s$	$1.04206(1.04217^{+0.00025}_{-0.00031})$	$1.04121(1.04145 \pm 0.00043)$	$1.04138(1.04138^{+0.00029}_{-0.00035})$
$f_{\rm EDE}$	⋯	$0.1183(0.119^{+0.023}_{-0.018})$	$0.1038(0.119 \pm 0.022)$
$\log_{10}(z_c)$	⋯	$3.571(3.568 \pm 0.034)$	$3.551(3.577 \pm 0.034)$
Ω_m	$0.2976(0.2977 \pm 0.0048)$	$0.2991(0.2923 \pm 0.0056)$	$0.2997(0.2936 \pm 0.0057)$
σ_8	$0.8017(0.8047 \pm 0.0060)$	$0.8329(0.8325 \pm 0.0083)$	$0.8260(0.8285^{+0.0085}_{-0.0075})$
S_8	$0.7985(0.8016^{+0.0096}_{-0.0080})$	$0.8316(0.822^{+0.011}_{-0.0093})$	$0.8256(0.820^{+0.014}_{-0.0080})$
$\Delta\chi^2_{\rm tot}$	⋯	-11.74	-13.78
ΔAIC	⋯	-5.74	-3.78

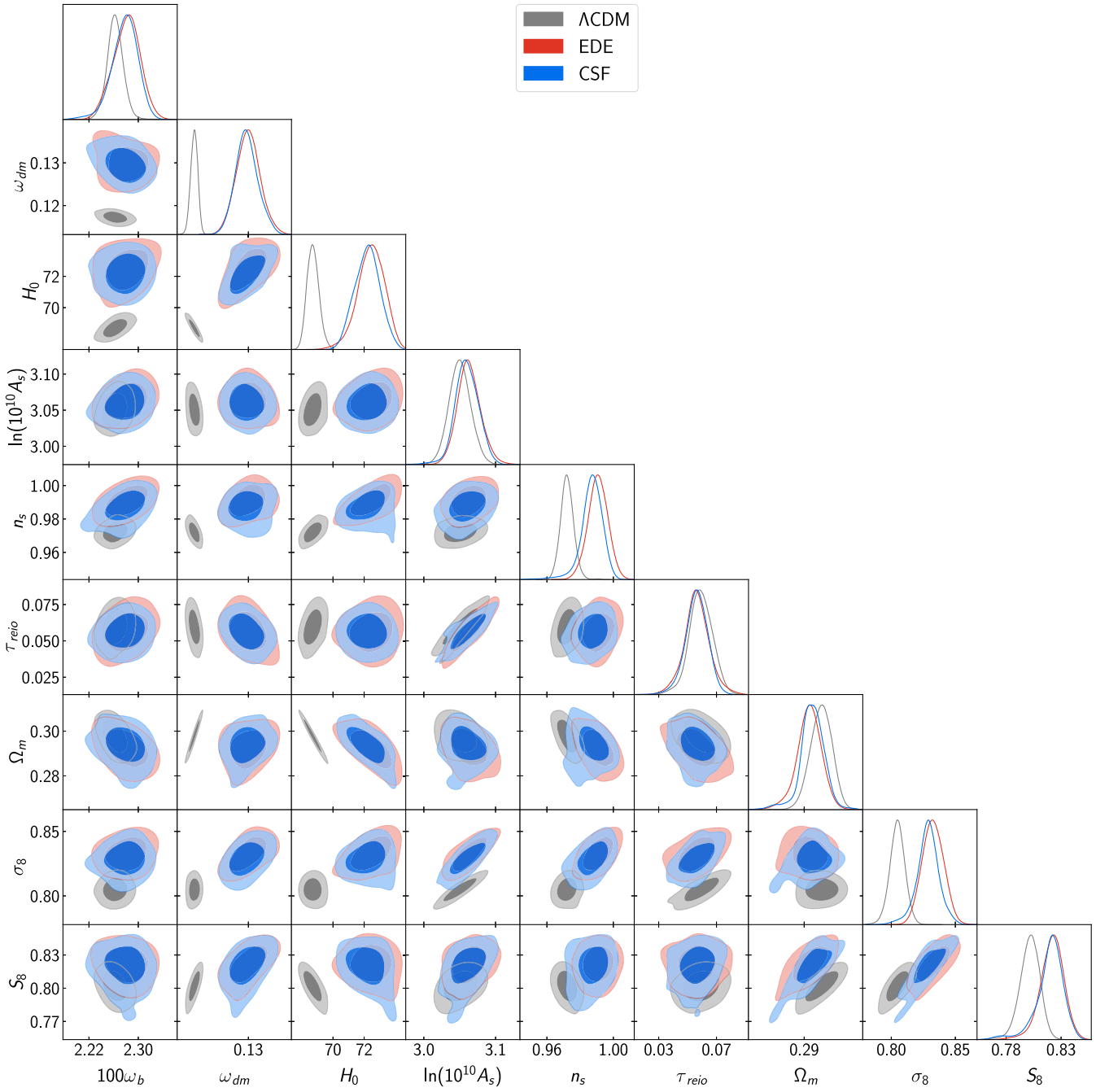

FIG. 7. The full Markov Chain Monte Carlo posteriors of various models were obtained by utilizing the entire dataset, including CMB, BAO, SNIa, SH0ES, and S_8 from DES-Y3.

[1] L. Verde, T. Treu, and A. G. Riess, Tensions between the early and late universe, Nat. Astron. **3**, 891 (2019).
[2] A. G. Riess, S. Casertano, W. Yuan, L. M. Macri, and D. Scolnic, Large magellanic cloud cepheid standards provide a 1% foundation for the determination of the Hubble constant and stronger evidence for physics beyond ΛCDM, Astrophys. J. **876**, 85 (2019).
[3] A. G. Riess, S. Casertano, W. Yuan, J. Bradley Bowers, L. Macri, J. C. Zinn, and D. Scolnic, Cosmic distances calibrated to 1% precision with gaia EDR3 parallaxes and

Hubble space telescope photometry of 75 Milky Way cepheids confirm tension with ΛCDM, Astrophys. J. Lett. **908**, L6 (2021).
[4] N. Aghanim, Y. Akrami *et al.* (Planck Collaboration), Planck 2018 results—VI. Cosmological parameters, Astron. Astrophys. **641**, A6 (2020).
[5] R. J. Cooke, M. Pettini, K. M. Nollett, and R. Jorgenson, The primordial deuterium abundance of the most metal-poor damped Lyman-alpha system, Astrophys. J. **830**, 148 (2016).
[6] N. Schöneberg, J. Lesgourgues, and D. C. Hooper, The BAO + BBN take on the Hubble tension, J. Cosmol. Astropart. Phys. 10 (2019) 029.
[7] E. Aubourg, S. Bailey, J. E. Bautista *et al.* (BOSS Collaboration), Cosmological implications of baryon acoustic oscillation measurements, Phys. Rev. D **92**, 123516 (2015).
[8] O. H. Philcox, M. M. Ivanov, M. Simonović, and M. Zaldarriaga, Combining full-shape and BAO analyses of galaxy power spectra: A 1.6% CMB-independent constraint on H_0, J. Cosmol. Astropart. Phys. 05 (2020) 032.
[9] A. G. Riess, W. Yuan, L. M. Macri *et al.*, A comprehensive measurement of the local value of the Hubble constant with 1 km/s/Mpc uncertainty from the Hubble space telescope and the SH0ES Team, Astrophys. J. Lett. **934**, L7 (2022).
[10] E. Macaulay, I. K. Wehus, and H. K. Eriksen, Lower Growth Rate from Recent Redshift Space Distortion Measurements Than Expected from Planck, Phys. Rev. Lett. **111**, 161301 (2013).
[11] H. Hildebrandt, F. Köhlinger, J. Busch *et al.*, Kids + viking-450: Cosmic shear tomography with optical and infrared data, Astron. Astrophys. **633**, A69 (2020).
[12] M. Asgari, C.-A. Lin, B. Joachimi *et al.*, Kids-1000 cosmology: Cosmic shear constraints and comparison between two point statistics, Astron. Astrophys. **645** (2020).
[13] C. Hikage, M. Oguri, T. Hamana *et al.*, Cosmology from cosmic shear power spectra with Subaru Hyper Suprime-Cam first-year data, Publ. Astron. Soc. Jpn. **71**, 43 (2019).
[14] T. M. C. Abbott, M. Aguena, A. Alarcon *et al.*, Dark energy survey year 3 results: Cosmological constraints from galaxy clustering and weak lensing, Phys. Rev. D **105**, 023520 (2022).
[15] E. D. Valentino, O. Mena, S. Pan, L. Visinelli, W. Yang, A. Melchiorri, D. F. Mota, A. G. Riess, and J. Silk, In the realm of the Hubble tension–a review of solutions, Classical Quantum Gravity **38**, 153001 (2021).
[16] X. Li and A. Shafieloo, A simple phenomenological emergent dark energy model can resolve the Hubble tension, Astrophys. J. Lett. **883**, L3 (2019).
[17] Z. Zhou, G. Liu, Y. Mu, and L. Xu, Can phantom transition at z 1 restore the Cosmic concordance?, Mon. Not. R. Astron. Soc. **511**, 595 (2022).
[18] V. Poulin, T. L. Smith, T. Karwal, and M. Kamionkowski, Early Dark Energy Can Resolve the Hubble Tension, Phys. Rev. Lett. **122**, 221301 (2019).
[19] T. L. Smith, V. Poulin, and M. A. Amin, Oscillating scalar fields and the Hubble tension: A resolution with novel signatures, Phys. Rev. D **101**, 063523 (2020).
[20] J. C. Hill, E. McDonough, M. W. Toomey, and S. Alexander, Early dark energy does not restore cosmological concordance, Phys. Rev. D **102**, 043507 (2020).
[21] M.-X. Lin, G. Benevento, W. Hu, and M. Raveri, Acoustic dark energy: Potential conversion of the Hubble tension, Phys. Rev. D **100**, 063542 (2019).
[22] F. Niedermann and M. S. Sloth, New early dark energy, Phys. Rev. D **103**, L041303 (2021).
[23] M. Kamionkowski, J. Pradler, and D. G. E. Walker, Dark Energy from the String Axiverse, Phys. Rev. Lett. **113**, 251302 (2014).
[24] D. J. Marsh, Axion cosmology, Phys. Rep. **643**, 1 (2016).
[25] E. McDonough, M.-X. Lin, J. C. Hill, W. Hu, and S. Zhou, Early dark sector, the Hubble tension, and the swampland, Phys. Rev. D **106**, 043525 (2022).
[26] G. D'Amico, L. Senatore, P. Zhang, and H. Zheng, The Hubble tension in light of the full-shape analysis of large-scale structure data, J. Cosmol. Astropart. Phys. 05 (2021) 072.
[27] M. Lucca, Multi-interacting dark energy and its cosmological implications, Phys. Rev. D **104**, 083510 (2021).
[28] J. Beltrán Jiménez, D. Bettoni, D. Figueruelo, F. A. Teppa Pannia, and S. Tsujikawa, Probing elastic interactions in the dark sector and the role of S_8, Phys. Rev. D **104**, 103503 (2021).
[29] L. O. Téllez-Tovar, T. Matos, and J. A. Vázquez, Cosmological constraints on the multiscalar field dark matter model, Phys. Rev. D **106**, 123501 (2022).
[30] E. G. M. Ferreira, Ultra-light dark matter, Astron. Astrophys. Rev. **29**, 1 (2021).
[31] C. Vafa, The string landscape and the swampland, arXiv: 0509212.
[32] E. Palti, The swampland: Introduction and review, Fortschr. Phys. **67**, 1900037 (2019).
[33] P. Agrawal, G. Obied, and C. Vafa, H_0 tension, swampland conjectures, and the epoch of fading dark matter, Phys. Rev. D **103**, 043523 (2021).
[34] N. Aghanim, Y. Akrami, M. Ashdown *et al.*, Planck 2018 results. V. CMB power spectra and likelihoods, Astron. Astrophys. **641**, A5 (2020).
[35] N. Aghanim, Y. Akrami, M. Ashdown *et al.*, Planck 2018 results—VIII. Gravitational lensing, Astron. Astrophys. **641**, A8 (2020).
[36] S. Alam, M. Ata, S. Bailey *et al.*, The clustering of galaxies in the completed SDSS-III baryon oscillation spectroscopic survey: Cosmological analysis of the DR12 galaxy sample, Mon. Not. R. Astron. Soc. **470**, 2617 (2017).
[37] M. A. Buen-Abad, M. Schmaltz, J. Lesgourgues, and T. Brinckmann, Interacting dark sector and precision cosmology, J. Cosmol. Astropart. Phys. 01 (2018) 008.
[38] F. Beutler, C. Blake, M. Colless, D. Heath Jones, L. Staveley-Smith, L. Campbell, Q. Parker, W. Saunders, and F. Watson, The 6df galaxy survey: Baryon acoustic oscillations and the local Hubble constant, Mon. Not. R. Astron. Soc. **416**, 3017 (2011).
[39] A. J. Ross, L. Samushia, C. Howlett, W. J. Percival, A. Burden, and M. Manera, The clustering of the SDSS DR7 main galaxy sample-I. A 4 percent distance measure at $z = 0.15$, Mon. Not. R. Astron. Soc. **449**, 835 (2015).
[40] D. M. Scolnic, D. O. Jones, A. Rest, Y. C. Pan *et al.*, The complete light-curve sample of spectroscopically confirmed SNe ia from pan-STARRS1 and cosmological constraints from the combined pantheon sample, Astrophys. J. **859**, 101 (2018).

[41] J. Beyer and C. Wetterich, Small scale structures in coupled scalar field dark matter, Phys. Lett. B **738**, 418 (2014).
[42] L. Amendola and R. Barbieri, Dark matter from an ultra-light pseudo-Goldsone-Boson, Phys. Lett. B **642**, 192 (2006).
[43] L. A. Ureña-López and A. X. Gonzalez-Morales, Towards accurate cosmological predictions for rapidly oscillating scalar fields as dark matter, J. Cosmol. Astropart. Phys. 07 (2016) 048.
[44] E. J. Copeland, A. R. Liddle, and D. Wands, Exponential potentials and cosmological scaling solutions, Phys. Rev. D **57**, 4686 (1998).
[45] L. A. Ureña-López, New perturbative method for analytical solutions in single-field models of inflation, Phys. Rev. D **94**, 063532 (2016).
[46] B. Wang, E. Abdalla, F. Atrio-Barandela, and D. Pavón, Dark matter and dark energy interactions: Theoretical challenges, cosmological implications and observational signatures, Rep. Prog. Phys. **79**, 096901 (2016).
[47] K. Koyama, R. Maartens, and Y.-S. Song, Velocities as a probe of dark sector interactions, J. Cosmol. Astropart. Phys. 10 (2009) 017.
[48] W. Yang, S. Pan, and D. F. Mota, Novel approach toward the large-scale stable interacting dark-energy models and their astronomical bounds, Phys. Rev. D **96**, 123508 (2017).
[49] A. Mukherjee and N. Banerjee, In search of the dark matter dark energy interaction: A kinematic approach, Classical Quantum Gravity **34** (2016).
[50] G. Olivares, F. Atrio-Barandela, and D. Pavón, Dynamics of interacting quintessence models: Observational constraints, Phys. Rev. D **77**, 063513 (2008).
[51] P. G. Ferreira and M. Joyce, Cosmology with a primordial scaling field, Phys. Rev. D **58**, 023503 (1998).
[52] W. Hu, Structure formation with generalized dark matter, Astrophys. J. **506**, 485 (1998).
[53] J. Lesgourgues, The cosmic linear anisotropy solving system (CLASS) I: Overview, arXiv:1104.2932.
[54] D. Blas, J. Lesgourgues, and T. Tram, The cosmic linear anisotropy solving system (CLASS). Part II: Approximation schemes, J. Cosmol. Astropart. Phys. 07 (2011) 034.
[55] F. X. L. Cedeño, A. X. González-Morales, and L. A. Ureña-López, Cosmological signatures of ultralight dark matter with an axionlike potential, Phys. Rev. D **96**, 061301 (2017).
[56] L. Kazantzidis and L. Perivolaropoulos, Evolution of the $f\sigma_8$ tension with the $Planck15\Lambda$CDM determination and implications for modified gravity theories, Phys. Rev. D **97**, 103503 (2018).
[57] B. Stölzner, A. Cuoco, J. Lesgourgues, and M. Bilicki, Updated tomographic analysis of the integrated Sachs-Wolfe effect and implications for dark energy, Phys. Rev. D **97**, 063506 (2018).
[58] B. Audren, J. Lesgourgues, K. Benabed, and S. Prunet, Conservative constraints on early cosmology with MONTEPYTHON, J. Cosmol. Astropart. Phys. 02 (2013) 001.
[59] A. Lewis, GetDist: A Python package for analysing Monte Carlo samples, arXiv:1910.13970.
[60] A. Gelman and D. B. Rubin, Inference from iterative simulation using multiple sequences, Stat. Sci. **7**, 457 (1992).
[61] H. Akaike, A new look at the statistical model identification, IEEE Trans. Autom. Control **19**, 716 (1974).